



# Functional palladium tetrapod core of heterogeneous palladium–platinum nanodendrites for enhanced oxygen reduction reaction

Trung-Thanh Nguyen<sup>a</sup>, Chun-Jern Pan<sup>a</sup>, Jyong-Yue Liu<sup>a</sup>, Hung-Lung Chou<sup>b</sup>, John Rick<sup>a</sup>, Wei-Nien Su<sup>b,\*</sup>, Bing-Joe Hwang<sup>a,c,1</sup>

<sup>a</sup> Department of Chemical Engineering, National Taiwan University of Science and Technology, 43 Keelung Road, Taipei 106, Taiwan

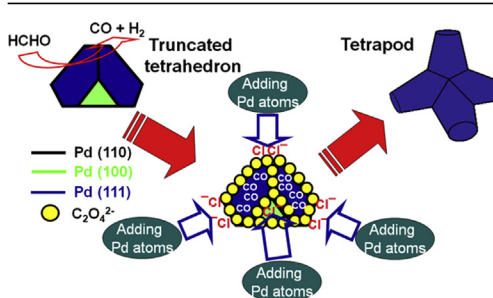
<sup>b</sup> Graduate Institute of Applied Science and Technology, National Taiwan University of Science and Technology, 43 Keelung Road, Taipei 106, Taiwan

<sup>c</sup> National Synchrotron Radiation Research Center, 101 Hsin-Ann Road, Hsinchu 30076, Taiwan

## HIGHLIGHTS

- A hydrothermal synthesis for preparing Pd nanotetrapods without toxic chemicals.
- Formation of Pd nanocrystals under different conditions was discussed.
- Pd-core of stepped surfaces ideal for growing dendritic Pt-shell with high activity.
- Pd tetrapods are as a functional morphology to enhance Pt shell's ORR activity.
- Pd<sub>tetrapod</sub>@30 wt% Pt showed the highest mass activity and stability for ORR.

## GRAPHICAL ABSTRACT



## ARTICLE INFO

### Article history:

Received 24 September 2013

Received in revised form

8 November 2013

Accepted 25 November 2013

Available online 7 December 2013

### Keywords:

Palladium–platinum core shell

Tetrapod

Dendrite

Heterogeneous structure

Oxygen reduction reaction

PEM fuel cells

## ABSTRACT

The synthesis, characterization, and application of bimetallic Pd–Pt nanocatalysts with heterogeneous structures are reported. The Pd tetrapod core is demonstrated to enhance the catalytic activity and durability of Pd@Pt nanodendrites for the oxygen reduction reaction (ORR). Special attention is given to the effects of oxalate-ion–formaldehyde during the hydrothermal synthesis of various Pd morphologies at different temperatures. Pd tetrapod synthesis can be delicately achieved without directly using hazardous CO gas. 30 wt% Pt on tetrapodal and truncated-octahedral Pd cores and 50 wt% Pt on tetrapodal Pd cores are prepared and compared against the commercial Pt/C catalyst (E-Tek) for ORR. The Pd<sub>tetrapod</sub>@30 wt% Pt catalyst exhibits the highest ORR activity. Overall, the Pd tetrapod core is a functional morphology which offers high-index facets for the subsequent deposition of Pt(110) nanodendrites, with the bimetallic interaction between two materials allowing for good electron transfer from the Pd core onto the Pt surfaces. Both effects contribute to the increased catalytic activity of Pd<sub>tetrapod</sub>@30 wt% Pt, even under a lower loading of Pt. Furthermore, Pd<sub>tetrapod</sub>@30 wt% Pt has a rather large particle size (~39.5 nm) which enhances durability and resistance to the agglomeration of Pt.

© 2013 Elsevier B.V. All rights reserved.

## 1. Introduction

For polymer electrolyte membrane fuel cells (PEMFC), a slow oxygen reduction reaction (ORR) is one of the issues requiring improvement [1,2]. Pt is the most efficient and widely used catalyst known for the ORR. However, Pt suffers from poisoning associated

\* Corresponding author. Fax: +886 2 27376922.

E-mail addresses: [wusu@mail.ntust.edu.tw](mailto:wusu@mail.ntust.edu.tw), [weinien.su@gmail.com](mailto:weinien.su@gmail.com) (W.-N. Su), [bjh@mail.ntust.edu.tw](mailto:bjh@mail.ntust.edu.tw) (B.-J. Hwang).

<sup>1</sup> Fax: +886 2 27376644.

with electrolytes and the hydroxyl layer, which limits the ORR kinetics and its long-term stability. Factors such as size, morphology, and composition controls of Pt particles have been extensively studied in the past decades in the search for a higher ORR activity, long-term stability and reduced Pt consumption [2–13].

Recent studies have shown that the improved catalytic properties could be attributed to relatively large surface areas and the presence of particularly active facets on Pt nanocrystals supported on metal nanoparticles [14–16]. The seed-mediated growth method has been used in the synthesis of such Pt-based heteronanostructures, because this technique can enable the formation of metallic nanostructures with precisely controlled morphologies and compositions [17–20]. Additionally, the morphology of seeds and corresponding exposed facets have a great influence on the nucleation and growth of the deposited metal and thus determine the structural and catalytic properties of the resultant nanostructures [6]. However, the morphologies of seeds applied thus far have been limited to low-index facets [6,16,19]. For example, Xia and co-workers showed that Pt dendrites on truncated octahedral Pd cores (including Pd(111) and Pd(100) planes) exhibited higher electrocatalytic activities and stabilities toward ORR than that of Pt/C (E-TEK) [16], while the contributions of cores with multi-pod morphologies and/or concave surfaces to inherent ORR activity and durability of Pt-based nanodendrites have not yet been revealed.

Generally speaking, smaller nanocatalysts show higher activities than larger ones, but electrocatalyst durability is directly proportional to the particle size [21]. Recently, a tetrapod morphology of CdTe nanoparticles was synthesized and applied to optoelectronic applications [22]. For the tetrapod morphology, the contact surface area is almost equal to the sum of the surface areas of four small particles with the size of individual branches in a nanotetrapod. From this viewpoint, nanotetrapods exhibit excellent contact surface areas and stepped planes for high activity, as well as a large particle size required for improved durability. As a result, the tetrapod shape can be seen as a functional morphology as a metal core for heteronanostructures of Pt-based nanocrystals. For Pt nanodendrites, Lee et al. showed that nanocatalysts with a particle size of between 15 nm and 30 nm exhibited higher catalytic activities and stabilities than that of Pt/C (E-Tek) [21]. In addition, Pd–Pt heteronanostructures showed superior catalytic activity for ORR [7,15,17,23]. The reaction kinetics of the synthesis of nanocrystals can be controlled by reagent concentration, pH of the precursor solution, temperature, type of reductant, addition of ionic species or a combination of these factors, but complications among these reaction parameters further increases the difficulty in controlling the reaction. Therefore, it is challenging to implement adequate kinetic control to produce nanocrystals with unusual morphologies, including those with high-energy facets and/or a negative curvature on the surface [15,19,24–28]. It is worth noting that  $\text{Na}_2\text{C}_2\text{O}_4$  and HCHO are used as the (111)-facet selective agent and reductant in the synthesis of alloyed Pd–Pt nanotetrahedra [29]. Shape-controlled synthesis of Pd nanocrystals (e.g., spheres, tetrahedra and multipods) is also successfully developed in the presence of oleylamine and alkylammonium alkylcarbamate as chelating agents using a  $\text{Pd}^{2+}$  precursor to control the reaction kinetics [30]. In these two examples, the control over the reduction kinetics by adding facet-selective agents to disturb the growth of seed allows for controlling the shape of noble metal nanocrystals. Thus, it is believed that the combination of selected-facet adsorbates and temperature can be employed to effectively control the facet growth for producing tetrapod nanoparticles.

In this work, Pd nanotetrapods were prepared and used as cores in Pd–Pt multipod dendritic (or flower-like Pd–Pt dendritic) nanocrystals, using a seed-mediated method, while Pd nanotetrapods were synthesized by a hydrothermal method in the

presence of HCHO, PVP, and  $\text{C}_2\text{O}_4^{2-}$  ions as the reductant, stabilizer, and efficient facet-selective agent, respectively. It was found that the presence of oxalate ions and formaldehyde along with a suitable temperature are key to the successful formation of Pd(111) nanotetrapods. The dendritic Pt shells were grown directly on tetrapodal Pd cores in the presence of ascorbic acid as a reductant (see [Experimental section](#)) with the slow addition of a  $\text{PtCl}_6^{2-}$  ion precursor. The electrochemical properties of the materials were examined to evaluate the effects of the morphologies of various Pd nanocores (e.g., truncated octahedrons and tetrapods) and shell thickness on their catalytic activity and stability during the ORR. The target of this work was to explore the synthesis of Pd nanotetrapods and highlight the advantages of the tetrapod Pd core compared to catalysts using truncated octahedral Pd cores with flat facets.

## 2. Experimental

### 2.1. Synthesis of Pd nanocubes

Pd nanocubes were synthesized by adding  $\text{K}_2\text{PdCl}_4$  solution into a mixture of ascorbic acid (AA), KBr, and NaCl according to a previously published method [16,31]. In a typical synthesis, aqueous solutions (8.0 mL) containing polyvinylpyrrolidone (PVP) (105 mg), AA (60 mg) and different amounts of KBr (5 mg) and NaCl (185 mg) were placed in a vial preheated to 90 °C in a stirred oil bath for 10 min. Next, an aqueous solution (3.0 mL) containing  $\text{KPdCl}_4$  (57 mg) was added using a pipette. After the vial had been capped, the reaction was allowed to continue at 90 °C for 3 h. The products were collected by centrifugation, washed several times with deionized (DI) water to remove excess PVP and redispersed in 11 mL of water to form the Pd nanocubes (~10 nm).

### 2.2. Synthesis of Pd truncated octahedrons

The procedure for the synthesis of Pd truncated octahedrons, from small Pd nanocubes in the presence of KI, was adapted from the work of Niu et al. [32]. In a typical synthesis of Pd truncated octahedrons, aqueous  $\text{KPdCl}_4$  solution (9.5 mg/3 mL of DI water) was added into an aqueous solution (8 mL) containing PVP (105 mg), HCHO (100  $\mu\text{L}$ ), cubic Pd seeds (1 mL of Pd cube (~10 nm) solution) and DI water at 60 °C with magnetic stirring (400 rpm). After 3 h of heating, the vial was removed from the oil bath and centrifuged to collect the product, which was washed three times with water and redispersed in DI water (4 mL) [32].

### 2.3. Synthesis of Pd tetrapods

In a typical synthesis, formaldehyde (0.4 mL) was added into an aqueous solution (10 mL) containing  $\text{KPdCl}_4$  (12.5 mg),  $\text{Na}_2\text{C}_2\text{O}_4$  (100 mg) and PVP (16.6 mg). The pH of the solution was adjusted with 4 drops (~0.2 mL) of aqueous HCl (1:1); the total volume of the solution was kept at 15 mL. The resulting homogeneous light-yellow solution was transferred to a 25 mL Teflon-line stainless steel autoclave and sealed. The autoclave was then heated at 150 °C (after initial heating from ambient at 8 °C  $\text{min}^{-1}$ ) for 3 h before cooling to room temperature. The black nanoparticles were centrifuged in an acetone–ethanol mixture (15 mL, 1:1 in volume) and washed with ethanol/water several times. The product (average yield >80%) was redispersed in 4 mL of DI water.

### 2.4. Synthesis of Pd–Pt bimetallic nanocrystals with a dendritic structure

In a typical synthesis, 2 mL of an aqueous suspension of Pd nanocores (truncated octahedrons, tetrapods) and 7 mL of an

aqueous solution containing PVP (50 mg), AA (100 mg) and KBr (50 mg) were mixed in a glass vial. The mixture was heated to 80 °C in air with stirring (400 rpm). Meanwhile,  $\text{H}_2\text{PtCl}_6$  (17.2 mg or 28.4 mg) was dissolved in DI water (5 mL). The  $\text{H}_2\text{PtCl}_6$  suspension was injected into the solution containing PVP, KBr, and Pd nanocrystals by dropping with a micropipette (using 10  $\mu\text{L}$  for one drop). The solution was heated to 80 °C for 3 h in air, and the product was centrifuged and washed several times first with an ethanol/acetone (1:1) mixture and then with water.

Detailed information about the chemicals and materials used, material characterization, electrode preparation as well as the electrochemical measurements [7,33] can be found in the Supporting information.

### 3. Results and discussion

#### 3.1. Structure of Pd nanotetrapods

Fig. 1 shows TEM images of the Pd nanocrystals with tetrapod morphology synthesized by the hydrothermal method. As shown in Fig. 1A and Fig. S1 (Supporting Information, SI), the nanotetrapods consist of highly uniform four-armed star-like nanoparticles. The geometric form of the Pd nanoparticles in the inset of Fig. 1A shows that the angle formed from the continuous two-arms in the same plane was  $\sim 120^\circ$ ; the apex angle of each arm was measured as  $60^\circ$  and the concave angle ( $\alpha_1$ ) as  $39^\circ$  (see Fig. S1A). The material's morphology could be described as a concave nanoparticulate with four extended arms which were not oriented in the same plane. Consequently, the particles are designated as Pd nanotetrapods. The High-Resolution Transmission Electron Microscopy (HRTEM) image in Fig. S1B shows that the Pd nanotetrapods constitute a new morphology of Pd nanocrystals and that its body surfaces are enclosed by (111) planes. However, high-index facets (411) were also observed on the concave surfaces of the Pd nanotetrapods (Fig. 1B) and are represented by an atomic model shown in Fig. 1C and Fig. S2. The average size (tip-to-tip distance) of the Pd nanotetrapods was measured as  $\sim 29$  nm. Although nanotetrapods composed of single-crystalline Au [34] and metal (II–IV) semiconductors (e.g., CdSe, CdTe, ZnO) [22,35,36] have been observed in previous reports, it is worth noting that this Pd(111) tetrapod morphology differed significantly from the previous tetrapod models, which is close to the tetrapod model of the metal (II–IV) semiconductors. These reports revealed that the tetrapods can be fabricated in the presence of both cubic (zinc blende) and

hexagonal (wurtzite) phases. While the cubic structure is important for the creation of cores with four active sites for four arms, the hexagonal structure is essential for the anisotropic growth of each arm [35]. In this work, the exposed surfaces of as-prepared Pd nanotetrapods are enclosed by (111) planes. Though some truncated tips were observed in the TEM images of Pd tetrapods, a high overall yield of tetrapod morphology was achieved.

#### 3.2. Role of oxalate ions and reaction temperature on the synthesis of tetrapodal Pd nanocrystals

To better understand the role of oxalate ions and synthesis conditions on the resulting morphology, Pd nanocrystals were prepared under different conditions (i.e., without or decreasing  $\text{C}_2\text{O}_4^{2-}$  ion concentration and changing to higher reaction temperatures, while other parameters were kept according to the standard conditions for the synthesis of Pd nanotetrapods) and investigated by TEM (Fig. 2 and Fig. S3). In the absence of  $\text{C}_2\text{O}_4^{2-}$  ions (Fig. 2A–C), Pd nanotruncated octahedrons were obtained instead, and Pd nanotetrahedra (Fig. 2D) were observed at a higher reaction temperature (200 °C). However, a mixture of tetrapod, concave tetrahedron, and irregular shapes was observed with lower concentration of oxalate ions (see Fig. S3). These results demonstrate the importance of  $\text{C}_2\text{O}_4^{2-}$  ions and reaction temperature on the synthesis of Pd tetrapod nanocrystals. Scheme 1 shows the morphologies of the as-prepared Pd nanocrystals synthesized at the different conditions.

#### 3.3. Formation mechanism of Pd nanotruncated octahedra, tetrahedra, and tetrapods

Nucleation and growth are two very important stages in the controlled synthesis of nanocrystals [37–39]. Small adsorbates can assist the shape-control efficacy of Pd nanocrystals by disturbing the growth of seeds [40]. This could be attributed to the different initial seed morphologies, resulting from the reduced reaction rate of Pd precursors [30]. Pd(acetylacetonate)<sub>2</sub> has been used as a special Pd precursor for the synthesis of Pd nanocrystals [30,41,42]. Recently, Han et al. showed that the morphology of Pd nanocrystals could be controlled by using oleylamine (OA) and alkylammonium alkylcarbamate (AAAC). The ratio of OA and AAAC could influence the reduction reaction kinetics and accounts for the various final metal shapes promoted by different Pd seed morphologies [30]. In previous reports, it was shown that the Pd nanocrystals with octahedral, truncated octahedral, cuboctahedral, tetrahedral and concave tetrahedral morphologies were enclosed by (111) planes, using formaldehyde as a reductant [20,43]. The authors believed that formaldehyde acted as a relatively mild reducing agent or as an adsorbate onto the surfaces of the Pd nanocrystals [20,43]. However, the formation mechanism remains unclear.

Additionally, it was shown that formaldehyde on Pd surfaces is likely to decompose into CO and  $\text{H}_2$  [44], and that CO acts as a strong adsorbate on the Pd(111) and Pd(100) planes [45–47]. The formation of concave Pd polyhedra was attributed to the CO adsorption on Pd(111) planes from the decomposition of formaldehyde on Pd surfaces [40]. Zheng et al. also showed that electrochemical oxidation formic acid activity depended on the percentage of Pd(110) facets, and that the activity enhanced with increased percentage of Pd(110) planes [43]. It was indicated that formic acid can more easily adsorb onto (110) planes than (111) planes of Pd nanocatalysts. In addition, Barth et al. investigated the bonding and surface diffusion of 4-trans-2-(pyrid-4-yl-vinyl) benzoic acid on Pd(110) surfaces [48]. The fatty acid ligand was used to synthesize CdSe(220) quantum disks in a controlled manner and the morphological control was also found to be temperature-

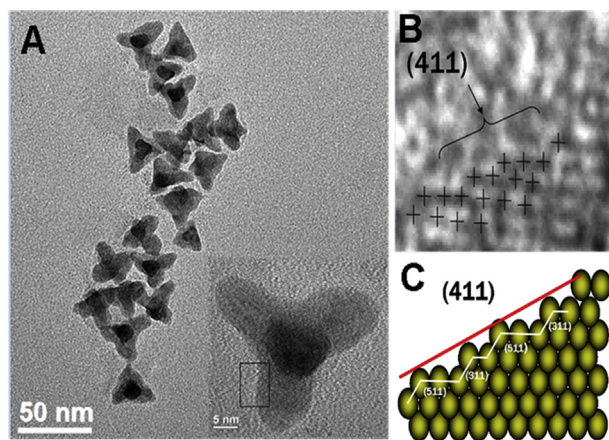
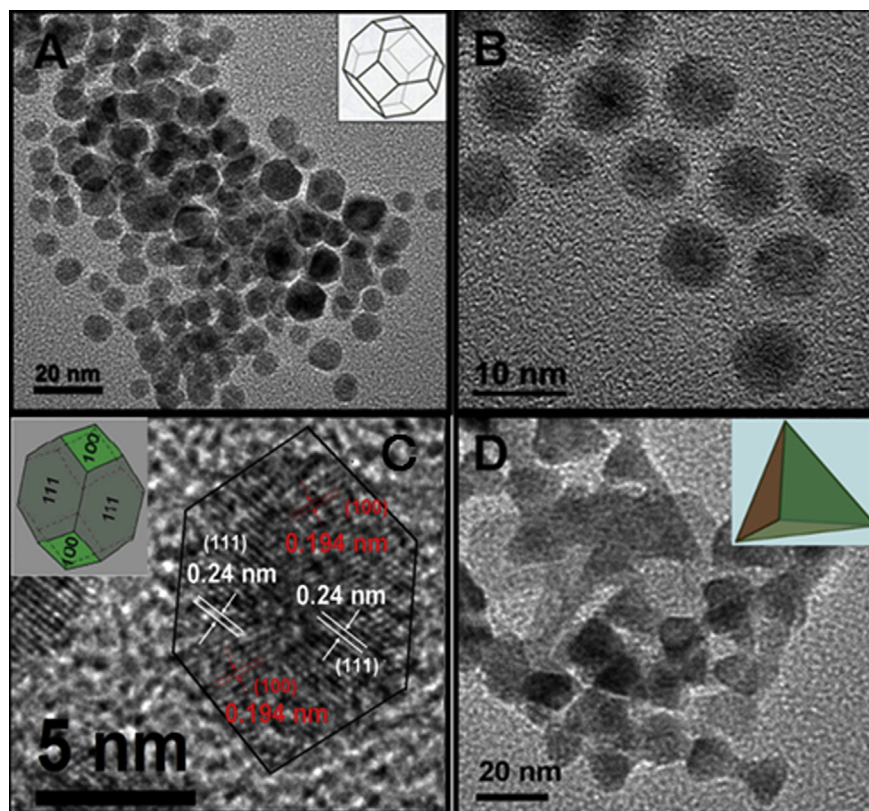


Fig. 1. (A) TEM image of Pd nanotetrapods and a magnified image (inset, scale bar = 5 nm); (B) HRTEM image of the inset region indicated by the box in (A), rotated 90°; and (C) a corresponding atomic model.





**Fig. 2.** TEM images of the Pd truncated octahedral (A–C, 150 °C) and tetrahedral (D) nanocrystals, synthesized under the same conditions as with the synthesis of Pd tetrapodal nanocrystals except for the absence of oxalate sodium (A–C) and at a reaction temperature of 200 °C (D).

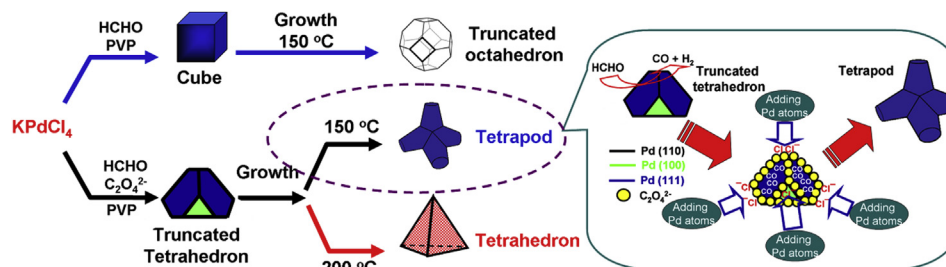
sensitive [49]. These examples imply that carboxylate groups might preferably adsorb onto Pd(110) planes.

Since the oxalate ion, carboxylate groups and acetylacetonate ligands share a similar structure, as shown in Scheme S1, the different morphologies of the as-prepared Pd nanocrystals (i.e., truncated octahedron and tetrahedron) are synthesized under the synergetic effects of oxalate ions and CO adsorption (from the decomposed formaldehyde). On the basis of the above-mentioned results, the nanocrystal growth mechanism is proposed as follows. In the absence of oxalate ions, the Pd truncated octahedra could grow from Pd nanocubes (see Fig. S4 in SI). Fresh Pd atoms are added onto the Pd(100) planes because of the strong adsorption of CO gas on the Pd(111) planes. In the presence of oxalate anions, the complex compound of  $\text{Pd}^{2+}$  precursor and oxalate anions was produced, and this complex compound could be reduced by formaldehyde at 150 °C, a much lower temperature than using  $\text{PdCl}_4^{2-}$  precursor. In this case, Pd nanotetrapods are successfully synthesized by growing fresh Pd atoms onto the (100) planes of the

truncated tetrahedral Pd seeds (see Fig. S5 in SI) since CO molecules are adsorbed onto the Pd(111) planes, while the Pd(110) planes are associated by coordinating  $\text{Pd}^{2+}$  ions and oxalate ions (as illustrated in Scheme 1). However, at 200 °C, tetrahedral Pd nanocrystals were obtained instead. One possible explanation would be that the rate of CO desorption increases and the monolayer of oxalate ligands on the (110) planes might become unstable at this elevated temperature. Overall, the combination of oxalate sodium and formaldehyde along with a proper thermal control proved to be successful in the synthesis of colloidal Pd nanotetrapods from truncated tetrahedral Pd seeds.

### 3.4. Pt Nanodendrites on various Pd core morphologies

Herein, the truncated octahedron morphology was taken as a shape reference to the tetrapod morphology, because the hetero-structural nanocrystal incorporating a Pt dendrite on a Pd truncated octahedron core showed a high activity for ORR [16]. It is noted that



**Scheme 1.** Structural development of Pd nanocrystals and the synthesis mechanism of Pd nanotetrapods.

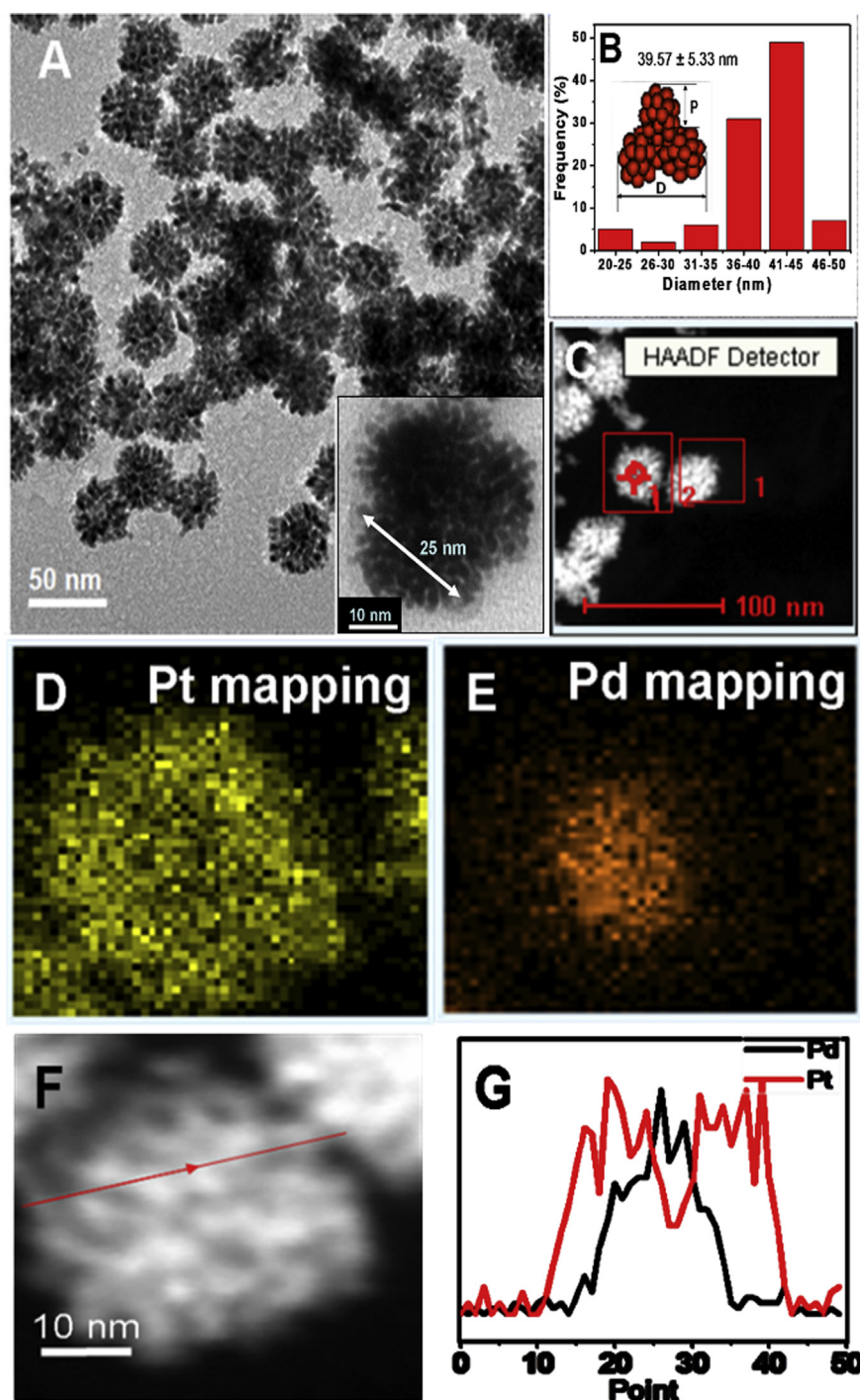


**Fig. 3.** Flower-like Pd<sub>4tetrapod</sub>@30 wt% Pt characterized by: (A, B) TEM; (C) HAADF-STEM; (D, E) elemental mapping; (F) HAADF-STEM (magnified view); and (G) cross-sectional composition line profiles.

truncated octahedral Pd nanocrystals have a similar size to the individual spots of tetrapodal Pd nanocrystals. The mechanism of formation for these Pd nanocrystals has been well-documented in the literature [17,41,43]. Truncated octahedral Pd nanocrystals were prepared by growing Pd metal onto cubic Pd seeds (shown in Fig. S6); the TEM images of the resulting truncated octahedral Pd nanocrystals are shown in Fig. S7. The XRD patterns obtained from the Pd cores (Fig. S8) show that their structures were face-centred cubic (FCC).

To study the effect of the core's morphology on the resulting Pd–Pt bimetallic nanocrystals, a dendritic Pt shell was prepared on different types of Pd cores (including truncated octahedron and tetrapod) using a seed-growth method. H<sub>2</sub>PtCl<sub>6</sub> was used as the source of Pt<sup>4+</sup> ions that acted as a precursor for the reduction reaction in which ascorbic acid was used to generate the dendritic Pt nanocrystals [6,14,50], while PVP was added to impede the aggregation of particles (see Experimental section for details). The synthetic method employed gave well-dispersed dendrites.

When the Pd nanotetrapods were employed as the Pd cores, a special morphology of the Pd–Pt bimetallic nanocrystals was observed, in which the four tips appear as flower-like nanoparticles with dendritic core–shell structures. Fig. 3A shows the TEM images of the Pd–Pt bimetallic nanocrystals with 30 wt% Pt. The size of the nanodendrites ranged from 20 to 50 nm (average diameter of  $39.57 \pm 5.33$  nm), as seen in Fig. 3B. The HAADF-STEM images, elemental mapping (Fig. 3C–F) and the TEM-line scan (Fig. 3G) confirmed that the structure of the Pd–Pt bimetallic nanocrystals consisted of a Pd core and a dendritic Pt shell, in which the size of each spot was  $\sim 25$  nm. The size of the flower-like nanoparticles at the tips (P, defined in the insert of Fig. 3B) was controllable by varying the Pt ratio. In case of 50 wt% Pt, the size of each pod was around 40 nm, as seen in Fig. S9.

The XRD patterns of Pd<sub>tetrapod</sub>@30 wt% Pt and Pd<sub>tetrapod</sub>@50 wt% Pt bimetallic nanocrystals are presented in Fig. 4. Owing to the similarity of Pd and Pt crystalline structures (JCPDS card No. 04-0802 (Pt) and No. 65-6174 (Pd)), the difference in the XRD peak positions for Pd and Pt is not distinct. The well-resolved peaks depicted in Fig. 4 could be indexed as being the (111), (200), (210) and (311) diffraction peaks, respectively. The spectra confirmed that all the synthesized nanoparticles have a highly crystalline face-centred-cubic phase with the Fm3m space group [14].

In addition, Pd<sub>trunc.octa</sub>@30 wt% Pt nanocrystals were also synthesized in this study for comparison, as compared using TEM images in Fig. S10. Inductively coupled plasma atomic emission spectroscopy (ICP-AES) analysis showed that the actual weight percentages of Pt were 30.7 and 35.4 wt% for nanotetrapods and nanotruncated octahedrons, respectively, when used as cores. The average thicknesses of the Pt shell were measured as around 5.2 and 6.7 nm for Pd<sub>tetrapod</sub>@30 wt% Pt and Pd<sub>trunc.octa</sub>@30 wt% Pt, respectively (see Table 1).

### 3.5. Functional morphology of Pd cores for ORR activity enhancements

The electrocatalytic activities of the Pd@Pt hetero-nanostructures towards the ORR were investigated and compared against a commercial sample comprising monometallic Pt nanoparticles on a carbon support as the reference (E-Tek, 20 wt% of 3.2 nm Pt nanoparticles on Vulcan XC-72 carbon support, Fig. S11 in SI). For all samples, the total loading of the metals (both Pd and Pt; or Pt for Pt/C) on glassy carbon electrode was  $42 \mu\text{g}_{\text{metal}} \text{cm}^{-2}$ . The geometric area of each rotating disk electrode (RDE) was  $0.196 \text{ cm}^2$ . The cyclic voltammetry (CV) curves exhibited potential regions

associated with  $\text{H}_{\text{upd}}$  adsorption and desorption processes ( $\text{H}^+ + \text{e}^- = \text{H}_{\text{upd}}$ ) from 0 to 0.4 V and reversible adsorption of  $\text{OH}_{\text{ad}}$  ( $2\text{H}_2\text{O} = \text{OH}_{\text{ad}} + \text{H}_3\text{O}^+ + \text{e}^-$ ) beyond 0.6 V, where  $\text{H}_{\text{upd}}$  and  $\text{OH}_{\text{ad}}$  refer to the under-potentially deposited hydrogen and the adsorbed hydroxyl species, respectively [51]. The electrochemically active surface area (ECSA) of the Pd–Pt catalyst was estimated by measuring the changes in the  $\text{H}_{\text{upd}}$  adsorption region only from 0.002 to 0.4 V, after double-layer correction, assuming a value of  $210 \mu\text{C cm}^{-2}$  for the adsorption of a hydrogen monolayer. The ECSA of the Pt/C catalyst was also calculated in the standard region from 0.02 to 0.4 V. The specific values of ECSA based on the Pt mass of Pd<sub>trunc.octa</sub>@30 wt% Pt, Pd<sub>tetrapod</sub>@30 wt% Pt, Pd<sub>tetrapod</sub>@50 wt% Pt and Pt/C were found to be 130.26, 212.94, 43.44, and  $71.17 \text{ m}^2 \text{ g}_{\text{Pt}}^{-1}$  and are summarized in Table 1. Fig. 5 shows the CV curves for the catalyst formed with different Pd core morphologies and also with different amounts of Pt.

The literature indicated that the specific facet of the seed associated with its shape plays a decisive role in the nucleation and growth of the shell. The overall effect determines the catalytic activity of heterogeneous nanostructures [6]. In  $\text{H}_2\text{SO}_4$  electrolyte solutions, Pt(100) nanocrystals usually show higher ORR activity than Pt(111) nanocrystals due to the adsorption of electrolyte species onto the specific planes of the Pt nanocrystals. Additionally, it was shown that the Pt catalyst with stepped surfaces (high-index planes) exhibits a higher catalytic ORR activity than that with basal low-index surfaces [52].

For Pd<sub>trunc.octa</sub>@30 wt% Pt catalyst (TEM images are shown in Fig. S10 in SI), the electrochemical properties of the Pt(111) and Pt(100) planes were also observed using CV measurements (Fig. 5A) in a  $\text{H}_2\text{SO}_4$  solution. The Pt(100) electrode showed a peak at 0.27 V, a characteristic presence of (100) planes. The small, broad peak at 0.45 V is associated with the transition in the adsorbed (bi)sulphate layers and disappeared as the (111) terrace width decreased [52]. The CV measurements show how the morphology of Pd nanotruncated octahedra affected the growth of the dendritic Pt shell and its resulting electrochemical properties. In Fig. 5B, for Pd<sub>tetrapod</sub>@30 wt% Pt catalyst, the CV peak at 0.19 V could be attributed to the hydrogen adsorption peak of the (110) planes on the dendritic Pt surface [53]. The shift in the peak towards a higher potential indicated an increase in the (110) terrace width; the increased number of (110) terraces also produced an increase in the current density [53]. Consequently, the different ECSA of Pt-based catalysts and even Pt/C (E-TEK) could be ascribed to the difference in the Pt planes on the catalyst surface. Further studies are necessary to explain how the Pt (110) planes are obtained on the dendritic Pd<sub>trunc.octa</sub>@Pt catalysts. In comparison, the Pd<sub>tetrapod</sub>@50 wt% Pt catalyst in Fig. 5C was characterized by a lower current density, indicating a decrease in the number of (110) terraces due to high Pt loading and increased agglomeration. Additionally, with higher Pt loading, Pd<sub>tetrapod</sub>@50 wt% Pt exhibited a 12 nm-thick dendritic Pt shell, greatly impeding the electron transfer from the Pd core to the Pt shell.

Catalytic activity with respect to the ORR was determined in  $\text{O}_2$ -saturated aqueous  $\text{H}_2\text{SO}_4$  (0.5 M) solutions using a glassy carbon RDE at room temperature at a sweep rate of  $10 \text{ mV s}^{-1}$  and a rotation rate of 1600 rpm. The polarization curves for the catalysts are shown in Fig. 6. The current densities ( $\text{j}/\text{mA cm}^{-2}$ ) were normalized to the geometric surface area of the glassy carbon (GC) electrode ( $0.196 \text{ cm}^2$ ). In this work, bare Pd cores with truncated octahedral and tetrapodal morphologies were not assessed for their ORR activity because the activity of Pd monometallic catalysts is known to be lower than those of Pd–Pt bimetallic catalysts [14]. As seen in Fig. 6, the core's geometry profoundly affected the activity of the hetero-nanostructures. The electrocatalytic activities of the different catalysts, estimated from the half-wave potential ( $E_{1/2}$ )

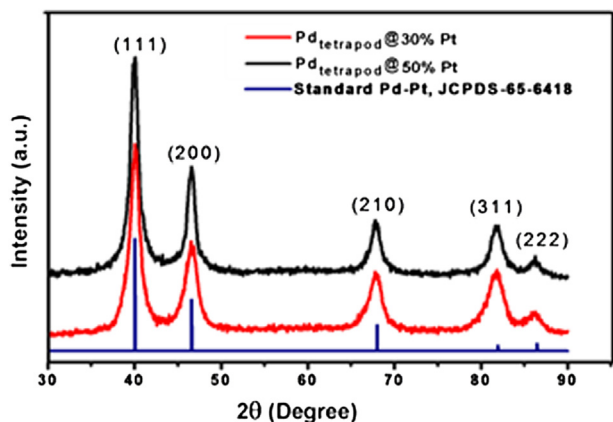


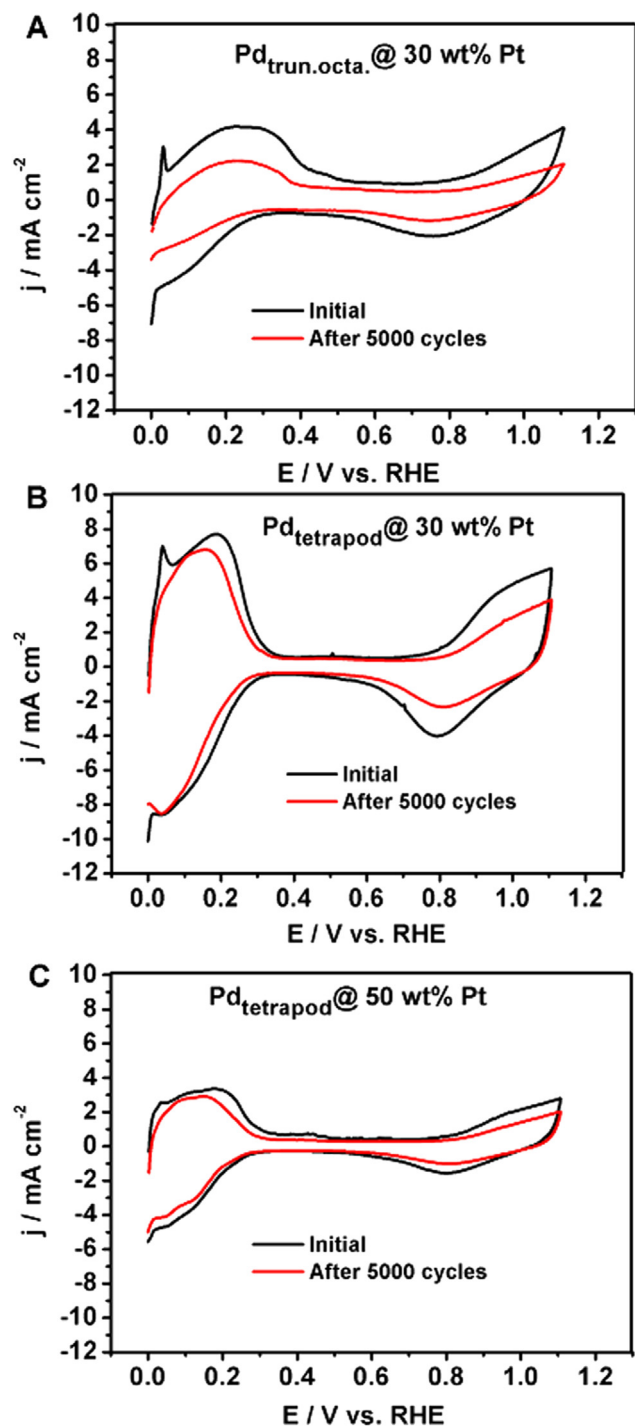
Fig. 4. XRD patterns of Pd–Pt bimetallic nanocrystals with dendritic Pt shell on Pd nanotetrapods.



**Table 1**

Average particle size of Pd core and Pd–Pt nanocrystals; summary of the Pt loading and resultant ECSA of Pd–Pt and E-Tek catalysts.

Catalyst	Size of Pd core (nm)	Size of Pd–Pt nanocrystal (nm)	Thickness of dendritic Pt shell (nm)	Pt Catalyst loading on GCE ( $\mu\text{g cm}^{-2}$ )	Specific ECSA ( $\text{m}^2 \text{g}^{-1}$ )
Pd <sub>trun.octa.</sub> @30 wt% Pt	16.7	30.1	6.7	12.6	130.26
Pd <sub>tetrapod</sub> @30 wt% Pt	29.0	39.5	5.2	12.6	212.94
Pd <sub>tetrapod</sub> @50 wt% Pt	29.0	53.0	12.0	21.0	43.44
20 wt% Pt/C (E-Tek)	—	3.2 nm Pt on Vulcan XC-72	—	42.0	71.17

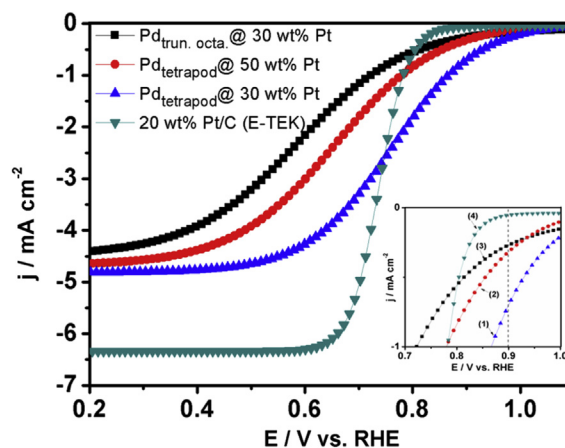
**Fig. 5.** Cyclic voltammetry durability tests for samples in  $\text{H}_2\text{SO}_4$  (0.5 M) before and after 5000 cycles at a scan rate of  $50 \text{ mV s}^{-1}$ . (A) Pd<sub>trun.octa.</sub>@30 wt% Pt; (B) Pd<sub>tetrapod</sub>@30 wt% Pt; (C) Pd<sub>tetrapod</sub>@50 wt% Pt.

[54], follows the order Pd<sub>tetrapod</sub>@30 wt% Pt > Pt/C > Pd<sub>tetrapod</sub>@50 wt% Pt > Pd<sub>trun.octa.</sub>@30 wt% Pt, with  $E_{1/2}$  values of 0.78, 0.74, 0.63 and 0.58 V, respectively. For a better understanding of the different ORR activities, the kinetic current associated with the intrinsic activity of the catalysts was obtained using a Koutecky–Levich equation for oxygen reduction with different catalysts (experimental details in the Supporting information) [55]. In order to compare the Pt mass activities for different catalysts, the kinetic current was calculated from the polarization curve by applying a mass transport correction and then normalizing with respect to the loading amount of Pt (Fig. 7A). At 0.9 V versus RHE, the mass activities for Pd<sub>tetrapod</sub>@30 wt% Pt, Pd<sub>trun.octa.</sub>@30 wt% Pt, Pd<sub>tetrapod</sub>@50 wt% Pt, and 20 wt% Pt/C (E-TEK) catalysts were 11.2, 5.8, 1.6, and 0.6  $\text{mA mg}_{\text{Pt}}^{-1}$ , respectively. Together with the observed  $E_{1/2}$  values and the catalytic stability (Figs. 5–7), these results show that the Pd<sub>tetrapod</sub>@30 wt% Pt nanocrystals outperformed Pd<sub>trun.octa.</sub>@30 wt% Pt, Pd<sub>tetrapod</sub>@50 wt% Pt, and Pt/C.

For ORR activity, the bimetallic Pd@Pt nanocrystals showed higher ORR mass activity than that of Pt/C (E-TEK). Unfortunately, due to the diluted solutions of Pd@Pt, we were unable to apply further characterization tools such as X-ray absorption spectroscopy for supporting analysis. It is believed that the electron transferring effect from the Pd metal core into the Pt surface plays a critical role, where the electronic interaction between Pt sites and  $\text{OH}^-$  groups was weakened, allowing the subsequently free Pt active sites to be made available, similar to the effect observed in our previous report [7]. As a result, the highest obtained ORR activity from Pd<sub>tetrapod</sub>@30 wt% Pt catalyst resulted from the presence of Pt(110) planes (high-index facets) on the catalyst surface.

### 3.6. Electrocatalytic stability toward the ORR

The catalytic stabilities were evaluated using both mass activity and ECSA calculations. After 5000 cycles, Pd<sub>tetrapod</sub>@30 wt% Pt still

**Fig. 6.** ORR polarization curves of dendritic Pt shells on Pd cores with different morphologies, different amounts of Pt on tetrapodal Pd cores and Pt/C (E-Tek) at  $25^\circ\text{C}$  in an  $\text{O}_2$ -saturated  $\text{H}_2\text{SO}_4$  (0.5 M) with an equivalent total mass of metals. The data were recorded at a scan rate of  $10 \text{ mV s}^{-1}$  and a rotation rate of 1600 rpm.

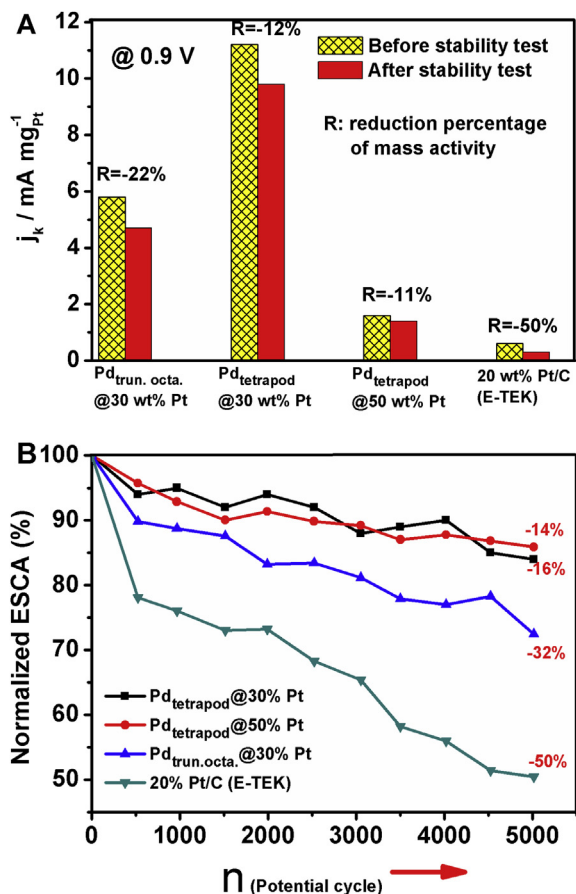


Fig. 7. (A) Mass activity of the catalysts before and after stability tests, normalized by weight of Pt at 0.9 V versus RHE; (B) Decreasing percentage of Pd–Pt electrocatalysts' ECSA as a function of number of potential cycles.

showed the highest mass activity at 0.9 V versus RHE, with a small reduction percentage of mass activity decrease stability among all the catalysts. The mass activity of Pd<sub>trun.octa</sub>@30 wt% Pt followed, though its mass activity was reduced by 22% after the stability test. The commercial reference Pt/C had the lowest mass activity before and after the stability test, as well as the greatest reduction of these values.

In terms of the normalized ECSA, compared to the original value, ECSAs of all catalysts inevitably decreased along with prolonged potential cycles, as shown in Fig. 7B. The decrease in the ECSA is believed to relate to the agglomeration and sintering of Pt during repetitive cycles. It is also generally recognized that the Pt–Pd interaction contributes to catalytic stability, whereas Pt/C is known to be less stable because of the weak interaction between the small nanoparticles and carbon support. Pd<sub>tetrapod</sub>@30 wt% Pt has a large and stable Pd core. At the same time, the loading of Pt was not excessive enough to cause an undesired agglomeration of Pt and decreased ECSA. The direct relationship between the particle size of Pd–Pt nanocrystals, Pd core size and the reduction percentage of mass activity and ECSA can be seen in Fig. 7B and is in a good agreement with previous results reported on the Pt dendrite system [21].

#### 4. Conclusions

We have demonstrated a simple and reproducible hydrothermal method for the synthesis of Pd nanocrystals with a new tetrapod morphology under the presence of non-toxic chemicals. The

interaction between oxalate ions and formaldehyde, and a proper temperature range facilitate the morphology control of Pd nanoparticles. During the growth process, small adsorbates, CO molecules (resulting from the decomposition of formaldehyde) and oxalate ions, would preferably adsorb onto the (111) and (110) planes of the truncated tetrahedral Pd seeds, respectively, to allow the favourable addition of fresh Pd atoms onto the Pd(100) planes. The tetrapod Pd nanocrystals can be successfully produced from the <100> directional growth at temperatures below 200 °C. The Pd<sub>tetrapod</sub>@30 wt% Pt catalyst showed the largest specific ECSA, mass activity and high stability for ORR among the other Pd<sub>trun.octa</sub>@30 wt% Pt, Pd<sub>tetrapod</sub>@50 wt% Pt, and Pt/C (E-TEK) catalysts on the basis of equivalent Pt mass. This work not only greatly advances our understanding of the formation mechanism of tetrapod Pd nanocrystals in the co-presence of oxalate ions and formaldehyde at a suitable temperature but also demonstrates the tetrapod Pd core as a functional morphology for enhancing catalytic activity and stability of Pd@Pt nanodendrites toward ORR. The tetrapod morphology provides stepped-surfaces (e.g., the (411) plane) for the growth of a dendritic Pt shell with large particle size. This tetrapod morphology concept can be extended to tailor other catalyst structures, or by changing metals in the tetrapod core and/or shell to improve performance for various purposes and applications.

#### Acknowledgements

We are grateful for financial support from the National Science Council (NSC 102-3113-P-011-001) and the Ministry of Education (Top Universities, 102H220401). We also thank to the National Center for High-Performance Computing and the Department of Chemical Engineering, National Taiwan University of Science and Technology (NTUST) for computer time and providing research facilities.

#### Appendix A. Supplementary data

Supplementary data related to this article can be found at <http://dx.doi.org/10.1016/j.jpowsour.2013.11.084>.

#### References

- [1] H.A. Gasteiger, S.S. Kocha, B. Sompalli, F.T. Wagner, *Appl. Catal. B Environ.* 56 (2005) 9–35.
- [2] J. Greeley, I.E.L. Stephens, A.S. Bondarenko, T.P. Johansson, H.A. Hansen, T.F. Jaramillo, J. Rossmeisl, I. Chorkendorff, J.K. Nørskov, *Nat. Chem.* 1 (2009) 552–556.
- [3] C. Wang, H. Daimon, T. Onodera, T. Koda, S. Sun, *Angew. Chem. Int. Ed.* 47 (2008) 3588–3591.
- [4] J. Wu, A. Gross, H. Yang, *Nano Lett.* 11 (2011) 798–802.
- [5] K. Yamamoto, T. Imaoka, W.-J. Chun, O. Enoki, H. Katoh, M. Takenaga, A. Sonoi, *Nat. Chem.* 1 (2009) 397–402.
- [6] Y. Kim, J.W. Hong, Y.W. Lee, M. Kim, D. Kim, W.S. Yun, S.W. Han, *Angew. Chem. Int. Ed.* 49 (2010) 10197–10201.
- [7] S.-H. Chang, W.-N. Su, M.-H. Yeh, C.-J. Pan, K.-L. Yu, D.-G. Liu, J.-F. Lee, B.-J. Hwang, *Chem. A Eur. J.* 16 (2010) 11064–11071.
- [8] F.-J. Lai, L.S. Sarma, H.-L. Chou, D.-G. Liu, C.-A. Hsieh, J.-F. Lee, B.-J. Hwang, *J. Phys. Chem. C* 113 (2009) 12674–12681.
- [9] M.D. Maciá, J.M. Campiña, E. Herrero, J.M. Feliu, *J. Electroanal. Chem.* 564 (2004) 141–150.
- [10] K. Sasaki, H. Naohara, Y. Cai, Y.M. Choi, P. Liu, M.B. Vukmirovic, J.X. Wang, R.R. Adzic, *Angew. Chem. Int. Ed.* 49 (2010) 8602–8607.
- [11] S.W. Lee, S. Chen, J. Suntivich, K. Sasaki, R.R. Adzic, Y. Shao-Horn, *J. Phys. Chem. Lett.* 1 (2010) 1316–1320.
- [12] F. Taufany, C.-J. Pan, J. Rick, H.-L. Chou, M.-C. Tsai, B.-J. Hwang, D.-G. Liu, J.-F. Lee, M.-T. Tang, Y.-C. Lee, C.-I. Chen, *ACS Nano* 5 (2011) 9370–9381.
- [13] F.-J. Lai, W.-N. Su, L.S. Sarma, D.-G. Liu, C.-A. Hsieh, J.-F. Lee, B.-J. Hwang, *Chem. A Eur. J.* 16 (2010) 4602–4611.
- [14] H. Zhang, Y. Yin, Y. Hu, C. Li, P. Wu, S. Wei, C. Cai, *J. Phys. Chem. C* 114 (2010) 11861–11867.
- [15] B. Lim, Y. Xia, *Angew. Chem. Int. Ed.* 50 (2011) 76–85.



- [16] B. Lim, M. Jiang, P.H.C. Camargo, E.C. Cho, J. Tao, X. Lu, Y. Zhu, Y. Xia, *Science* 324 (2009) 1302–1305.
- [17] S.E. Habas, H. Lee, V. Radmilovic, G.A. Somorjai, P. Yang, *Nat. Mater.* 6 (2007) 692–697.
- [18] D. Seo, C.I. Yoo, J. Jung, H. Song, *J. Am. Chem. Soc.* 130 (2008) 2940–2941.
- [19] H. Zhang, M. Jin, J. Wang, W. Li, P.H.C. Camargo, M.J. Kim, D. Yang, Z. Xie, Y. Xia, *J. Am. Chem. Soc.* 133 (2011) 6078–6089.
- [20] M. Jin, H. Zhang, Z. Xie, Y. Xia, *Energy Environ. Sci.* 5 (2012) 6352–6357.
- [21] C. Kim, J.-G. Oh, Y.-T. Kim, H. Kim, H. Lee, *Electrochem. Commun.* 12 (2010) 1596–1599.
- [22] A. Sugunan, S.H.M. Jafri, J. Qin, T. Blom, M.S. Toprak, K. Leifer, M. Muhammed, *J. Mater. Chem.* 20 (2010) 1208–1214.
- [23] H. Lee, S.E. Habas, G.A. Somorjai, P. Yang, *J. Am. Chem. Soc.* 130 (2008) 5406–5407.
- [24] H. Zhang, W. Li, M. Jin, J. Zeng, T. Yu, D. Yang, Y. Xia, *Nano Lett.* 11 (2010) 898–903.
- [25] X. Huang, Z. Zhao, J. Fan, Y. Tan, N. Zheng, *J. Am. Chem. Soc.* 133 (2011) 4718–4721.
- [26] T. Yu, D.Y. Kim, H. Zhang, Y. Xia, *Angew. Chem. Int. Ed.* 50 (2011) 2773–2777.
- [27] C.J. DeSantis, A.A. Peverly, D.G. Peters, S.E. Skrabalak, *Nano Lett.* 11 (2011) 2164–2168.
- [28] L. Zhang, J. Zhang, Q. Kuang, S. Xie, Z. Jiang, Z. Xie, L. Zheng, *J. Am. Chem. Soc.* 133 (2011) 17114–17117.
- [29] A.-X. Yin, X.-Q. Min, Y.-W. Zhang, C.-H. Yan, *J. Am. Chem. Soc.* 133 (2011) 3816–3819.
- [30] B. Hu, K. Ding, T. Wu, X. Zhou, H. Fan, T. Jiang, Q. Wang, B. Han, *Chem. Commun.* 46 (2010) 8552–8554.
- [31] M. Crespo-Quesada, J.-M. Andanson, A. Yarulin, B. Lim, Y. Xia, L. Kiwi-Minsker, *Langmuir* 27 (2011) 7909–7916.
- [32] W. Niu, L. Zhang, G. Xu, *ACS Nano* 4 (2010) 1987–1996.
- [33] K.M. Yeo, S. Choi, R.M. Anisur, *Angew. Chem. Int. Ed.* 50 (2011) 745–748.
- [34] S. Chen, Z.L. Wang, J. Ballato, S.H. Foulger, D.L. Carroll, *J. Am. Chem. Soc.* 125 (2003) 16186–16187.
- [35] L. Manna, E.C. Scher, A.P. Alivisatos, *J. Am. Chem. Soc.* 122 (2000) 12700–12706.
- [36] K. Sun, J. Qi, Q. Zhang, Y. Yang, Y. Zhang, *Nanoscale* 3 (2011) 2166–2168.
- [37] J. Park, J. Joo, S.G. Kwon, Y. Jang, T. Hyeon, *Angew. Chem. Int. Ed.* 46 (2007) 4630–4660.
- [38] A.R. Tao, S. Habas, P. Yang, *Small* 4 (2008) 310–325.
- [39] Y. Xia, Y. Xiong, B. Lim, S.E. Skrabalak, *Angew. Chem. Int. Ed.* 48 (2009) 60–103.
- [40] M. Chen, B. Wu, J. Yang, N. Zheng, *Adv. Mater.* 24 (2012) 862–879.
- [41] Z. Niu, Q. Peng, M. Gong, H. Rong, Y. Li, *Angew. Chem. Int. Ed.* 50 (2011) 6315–6319.
- [42] X. Huang, S. Tang, X. Mu, Y. Dai, G. Chen, Z. Zhou, F. Ruan, Z. Yang, N. Zheng, *Nat Nano* 6 (2011) 28–32.
- [43] X. Huang, S. Tang, H. Zhang, Z. Zhou, N. Zheng, *J. Am. Chem. Soc.* 131 (2009) 13916–13917.
- [44] G. Ertl, J. Tornau, *Z. Phys. Chem.* (1977) 301–308.
- [45] A.B. Anderson, M.K. Awad, *J. Am. Chem. Soc.* 107 (1985) 7854–7857.
- [46] W.K. Kuhn, J.S. Szanyi, D.W. Goodman, *Surf. Sci. Lett.* (1992) L611–L618.
- [47] J. Szanyi, W.K. Kuhn, D.W. Goodman, *J. Vac. Sci. Technol. A* 4 (1993) 1969–1974.
- [48] J. Weckesser, J.V. Barth, K. Kern, *J. Chem. Phys.* 110 (1999) 4.
- [49] Z. Li, X. Peng, *J. Am. Chem. Soc.* 133 (2011) 6578–6586.
- [50] L. Wang, Y. Nemoto, Y. Yamauchi, *J. Am. Chem. Soc.* 133 (2011) 9674–9677.
- [51] R. Gómez, J.M. Orts, B. Álvarez-Ruiz, J.M. Feliu, *J. Phys. Chem. B* 108 (2003) 228–238.
- [52] A. Kuzume, E. Herrero, J.M. Feliu, *J. Electroanal. Chem.* 599 (2007) 333–343.
- [53] J. Solla-Gullon, F.J. Vidal-Iglesias, A. Lopez-Cudero, E. Garnier, J.M. Feliu, A. Aldaz, *Phys. Chem. Chem. Phys.* 10 (2008) 3689–3698.
- [54] T. Ghosh, M.B. Vukmirovic, F.J. DiSalvo, R.R. Adzic, *J. Am. Chem. Soc.* 132 (2009) 906–907.
- [55] A.J. Bard, L.R. Faulkner, *Electrochemical Methods: Fundamentals and Applications*, Wiley, New York, 2000.